Anti-Icing Fluid Secondary Wave and Its Role in Lift Loss During Takeoff

Pekka Koivisto*

Aalto University, FI-00076 Aalto, Finland

Erkki Soinne†

Finnish Transport Safety Agency (Trafi), 00101 Helsinki, Finland

and

Juha Kivekäs‡

Arteform Ltd., FI-02150 Espoo, Finland

Effects of anti-icing fluid secondary wave on wing section lift degradation during simulated takeoff were studied in Aalto University 2 m × 2 m Low Speed Wind Tunnel during 2012–2014 and 2016–2017. The existence of secondary waves has been frequently reported since the first studies of anti-icing fluid effects on the wing lift degradation. However, the studies on its quantitative contribution to the lift degradation are scarce. The effects of wing section geometry and configuration on the secondary wave have not been addressed in the previous studies. In the present study two different wind tunnel models were used: a DLR-F15 wing section with a chord of 0.65 m and a modified HL-CRM wing section with a chord of 0.63 m. Both were two-dimensional three-element models. The lift coefficient measurements suggested that the secondary wave may have a dominating contribution to the fluid-induced lift degradation. The slat size and geometry turned out to have a significant effect on the formation and size of the secondary wave.

Nomenclature

C_l	=	lift coefficient, two-dimensional wing
C_L	=	lift coefficient, three-dimensional wing
C_m	=	pitching moment coefficient, two-dimensional wing
c	=	chord
k	=	roughness height
V_1	=	decision speed
$V_{1\,sg}$	=	1 g stalling speed
V_R	=	rotation speed
V_2	=	takeoff safety speed
x/c	=	chordwise relative coordinate (leading edge, x/c is equal to 0; trailing edge, x/c is equal to 1)
α	=	angle of attack

I. Introduction

PRESENT Aerodynamic Acceptance Test (AAT) for de/anti-icing fluids is defined in SAE Aerospace Standard AS 5900 [1]. The flight tests and extensive wind tunnel tests that formed the scientific basis of AAT consider predominantly lift coefficient degradation and its relation to boundary-layer displacement thickness growth caused by de/anti-icing fluids. The most significant research work performed to establish an acceptance test was carried out by Boeing [2,3], NASA Lewis Research Center [4], and Von Karman Institute for Fluid Dynamics [5–7]. The initial acceptance test was established for large aircrafts (rotation speed above 100 knots). Shortly after this there was research work done also on commuter aircraft to establish an acceptance test for aircrafts with rotation speed below 100 knots [8,9]. A comprehensive review of the research basis regarding the

aerodynamic acceptance test is given by Broeren and Riley [10]. The role of the so-called secondary waves on the fluid contamination-caused lift degradation were recognized already in the first studies on de/anti-icing fluids [11,12].

Secondary wave is a fluid wave appearing on the wing upper surface immediately after the start of rotation of an airliner during takeoff. The first hypothesis describing the formation process of a secondary wave was given probably by Hill and Zierten [11]: "*At the takeoff ground roll attitude the local pressure coefficients, hence velocities, are low near the wing's leading edge when compared to the local velocities at liftoff attitudes. The subsequent low shear stress during the takeoff ground acceleration is hypothesized to leave a film of fluid near the wing leading edge that is subsequently 'scrubbed' from the wing once the higher shear stress develops at the liftoff angle of attack. Also, movement of the wing's leading-edge stagnation line toward the lower surface as the angle of attack increases probably sheds fluid that had accumulated along the stagnation line during the takeoff acceleration ground roll. Capillary waves within the secondary gravity wave are apparently rough enough to cause the higher lift loss observed at the increased angles of attack.*"

Though several studies [11–13] report on evidence of secondary wave effect on lift degradation after rotation, it is difficult to isolate quantitatively the contribution of the secondary wave effect from other fluid effects. Perhaps the closest estimate is reported by Broeren et al. [13]. There is no visual evidence (photographic or videotape) of the secondary wave in [13], as the reasoning on its existence is done indirectly by measuring lift losses with fluid applied and/or wiped out to/from different areas on the wing. The interconnection between the secondary wave and lift degradation is often reported only qualitatively as in the following quote from Runyan et al. [12] may be realized (the wing section considered is B-737-200ADV wing section at 75% span location): "*Lift losses on the two-dimensional model with the flaps 15°, gapped-slat configuration are shown in . . . . These losses are much larger than those for the flaps 5°, sealed slat configuration. Secondary fluid waves were observed at both flap settings on the two-dimensional model immediately after rotation, just as had been observed on the three dimensional half model. The secondary waves were, again, larger for the flaps 15° configuration than for the flaps 5° configuration.*"

Hill and Zierten [11] point out that secondary wave effect is clearly configuration dependent as do Runyan et al. [12]. It should be noted that the wing section in [13] did not have a slat at all, whereas in

*Doctoral Student, Department of Mechanical Engineering, Sähkömiehentie 4.

†Chief Adviser Aeronautics, PL 320, Organization Services Department, Kumpulantie 9.

‡CEO, Sähkömiehentie 4.

[11,12] both slotted slat and sealed slat configurations were tested. Though the effect of the secondary wave and its dependency of the wing section geometry and configuration have been recognized, they have not been studied separately in detail in previous research. The purpose of this study is to fill this existing gap in the available publications.

In this study two different three-element wing sections are used to study the effects of the secondary wave on the lift degradation. Also, some visual analysis based on videotape recordings is included. For both wing sections, two different configurations in the slat position—retracted and sealed or extended—were applied to evaluate the effect of the secondary wave. In addition to this, a test with slat extended but anti-icing fluid applied only on the leading-edge area was conducted to isolate the effect of a secondary wave.

The present study applies the methodology adopted in the wind tunnel tests that formed the scientific basis of the present AAT [1]. This means simulated takeoff runs in a wind tunnel with accelerating airspeeds up to the speeds that correspond to a typical airliner rotation speed, and sequentially rotating the wing model to an angle of attack representing a lift coefficient typical in a One Engine Out situation at the speed of V_2. The aerodynamic degradation is determined by measuring forces acting on the wing model throughout the wind tunnel run.

II. Objectives

The objectives of the present study may be divided as follows:

1) To indicate the relationship between secondary wave visual observations and lift loss history

2) To assess the contribution of the secondary wave effect on the lift loss

3) To illustrate and analyze the differences of the secondary wave effect for two different wing section geometries, and for two different configurations

Using the two different wing section models with almost equal chord size and testing in the same wind tunnel incorporating the same type of support strut structure enabled a meaningful comparison of the results between the models. The two wing models represent clearly two different designs. The relative thicknesses and the slat design differ from each other, which appear to be relevant factors in the formation process of the secondary wave.

III. Experimental Setup

A. Wind Tunnel

Aalto University Low Speed Wind Tunnel is a closed-circuit wind tunnel with test section dimensions of 2 m × 2 m and test section length of 4 m. The flow uniformity in the test section is < 3.4%, and the turbulence level is < 0.28% at the wind tunnel speed of 60 m/s. As the measurements were performed in an accelerating airflow simulating an airplane takeoff run, the turbulence intensity of the wind tunnel was also determined during the acceleration. The maximum peak value of the turbulence level occurred at the very beginning of the acceleration period and was less than 0.6%. The temperatures in the test section follow roughly the daily outside air temperature (OAT), which during the tests of this study varied between 0 and 11°C.

B. Wing Section Models and Their Setup

The wing section model geometries have been chosen to represent two different transport airplane types of wing sections. The geometries of the wing sections are illustrated in Fig. 1. The main dimensions and other relevant data of the wing sections are collected in Table 1. Both models were equipped with slats and flaps to enable a takeoff configuration simulation. As the wing models were intended to be two-dimensional (2D), neither of them incorporated sweep or twist.

The DLR-F15 [14] geometry consisted of unambiguous 2D coordinates, whereas the HL-CRM Mod data were extracted from the three-dimensional (3D) wing geometry. The HL-CRM [15] section was taken from the wing at 50% span in a direction approximately
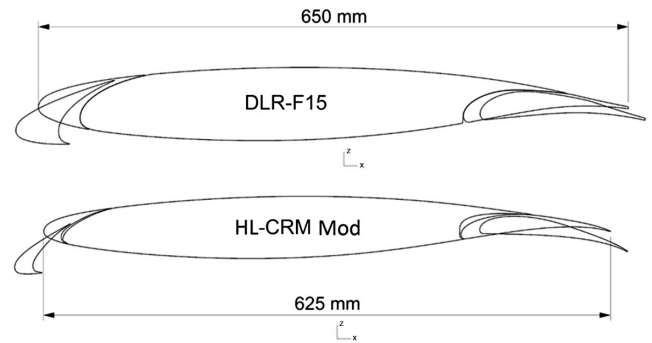

Fig. 1   The two wing sections used in the wind tunnel tests of present study. Clean and selected takeoff configurations presented—DLR-F15: slat 11°, flap 5°; HL-CRM Mod: slat 22°, flap 10°.

parallel to the local streamline. In addition, some minor modifications were made to this geometry to enable manufacturing and handling of the model. For this reason, the section is hereafter referred to as the "HL-CRM Mod" in this paper. As the selected wing section models differ clearly in thickness ratios and slat design from each other, they give a possibility to study the effect of the wing section geometry and configuration to the anti-icing fluid effects on lift coefficient during the takeoff sequence.

The wind tunnel is equipped with a three-component platform type external balance located above the test section ceiling. The wing models were mounted to the platform with three (DLR-F15) or four (HL-CRM Mod) vertical struts. Figure 2 illustrates the HL-CRM Mod wing section model setup. The two vertical front struts are identical in both wing section model assemblies. In HL-CRM Mod wing section model there are two vertical rear struts mounted directly to the end plates, whereas in DLR-F15 model one vertical rear strut is mounted to a horizontal strut connecting the end plates (Fig. 3). The rear strut setting enabled the model to be rotated about the pitch axis during the wind tunnel runs to simulate the takeoff sequence.

The models were equipped with endplates to minimize the three-dimensionality of the flow (Figs. 2 and 3). A reasonable two-dimensionality and absence of flow separations were confirmed by tufts. Slats and flaps were adjustable in both models to enable simulation of the real operational sequence, where the flaps and slats are extended after anti-icing treatment just before the takeoff.

IV. Data Acquisition and Assessment of Measurement Accuracy

A standard measuring software collects the wind tunnel temperature, airspeed, dynamic pressure, relative humidity, balance forces and moments (lift, drag, and pitching moment in this case), and wing angle of attack. For qualitative analysis of the fluid flow off and secondary wave movement, the test runs were videotaped through a Plexiglas window on the ceiling of the test section. The events on the lower surface of the wing section were also videotaped through the transparent test section door.

The wind tunnel tests with an anti-icing treatment were conducted using only one Type IV fluid. The initial mean thicknesses of fluid layers were defined by pointwise measurements (27 evenly spaced points) of film thickness using a thickness gauge. The resolution of the thickness gauge was 25–50 μm depending on the scale. Fluid treatment in the tests resulted to a mean initial fluid thickness of 1.0 mm with deviation of ±0.1 mm. The maximum effect of mass of the applied fluid on the measured lift values was then less than 0.1% of the lift force. Moreover, most of the fluid has left the upper surface

Table 1   Information on the wing sections selected to the study

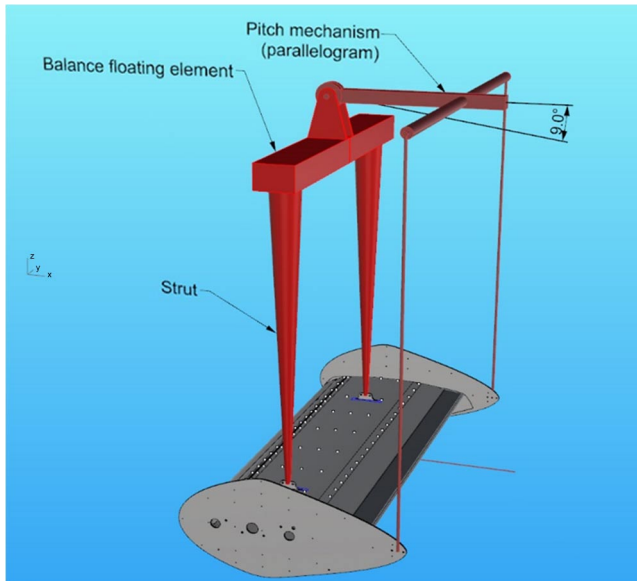| Wing section	Chord, m	Span, m	Area, m^2	Thickness, %
DLR-F15	0.65	1.50	0.975	15.0
HL-CRM Mod	0.63	1.55	0.969	10.9

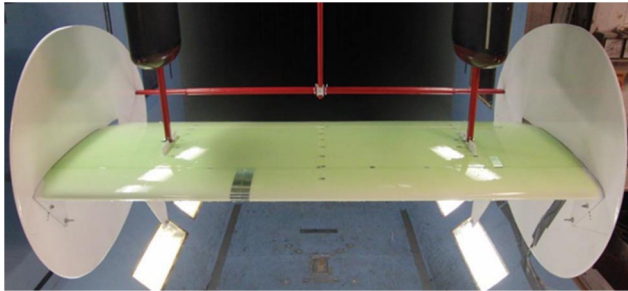**Fig. 2 Wind tunnel balance setup and HL CRM Mod model mounting and endplates.**

Fig. 3 Mounting and endplates of wing section model DLR-F15.

at the significant point of rotation, which means that the effect of fluid mass is insignificant in this study.

The effect of anti-icing treatments on the takeoff performance was evaluated by measuring the lift coefficient degradation ΔC_l due to the contamination. This means sequential C_l—measurements of an uncontaminated (cleaned) wing and a fluid-contaminated wing. The lift coefficient measurements for an uncontaminated DLR-F15 wing gave for 20 clean wing tests a mean value of 1.281 with a standard deviation of 0.0028. For the HL-CRM Mod wing section with the 12 measurements done for uncontaminated wing at takeoff angle of attack, the lift coefficient mean value was 1.501 with a standard deviation of 0.0037. For an anti-ice treated wing the lift coefficient repeatability was not as good. Just after rotation the standard deviation of lift coefficient for 2–4 runs with similar anti-icing treatment varied for both wing section models between 0.005 and 0.01. The obvious reason for higher standard deviation figures is the difficulty to repeat all the conditions of the fluid applications.

An uncertainty analysis was accomplished for the lift coefficient data with a 95% confidence level (equals to $20:1$ odds). The measured variables include the dynamic pressure of the test section flow, the balance loads, and the angle of attack. The lift coefficient is determined at a constant angle of attack (Table 2), and so the uncertainty of the specific angle of attack only is considered. The uncertainty of the angle of attack is based on inclinometer measurement that had an uncertainty of ± 0.017 deg. The test section dynamic pressure transducer accuracy was of ± 1 Pa. Combined to pitot tube axis misalignment error the total uncertainty of the dynamic pressure at wind tunnel speed of 60 m/s was $\pm 0.22\%$. The total uncertainty of the lift force at the maximum actual output was $\pm 0.05\%$. At the speed of 60 m/s and at the specified angle of attack (Table 2), the total instrumentation uncertainty was $\pm 0.23\%$. When combining the instrumentation errors to the standard deviations of the uncontaminated lift coefficients above, the total uncertainties are $\pm 0.006 (\pm 0.49\%)$ for DLR-F15 and $\pm 0.008 (\pm 0.54\%)$ for HL-CRM Mod (Table 2).

V. Measurement Program

Considering anti-icing fluid–induced wing contamination–related performance degradation, the most critical condition is the One Engine Inoperative (OEI) situation where the airliner is flying at the speed of V_2 after lift-off up to the so-called cleaning altitude at which the flaps and slats are retracted (>400 ft above ground level as per EASA CS 25.121). As the performance degradation due to anti-icing treatment has practically diminished well before reaching the cleaning altitude, the relevant phases of flight regarding performance degradation are the takeoff roll and initial climb at speed V_2.

The assessment of the effect of anti-icing treatment–related contamination on the wing was in this study decided to be done in line with the research work done while developing the present AAT. For this reason, the wind tunnel tests were designed to simulate the takeoff as follows: the wind tunnel is first accelerated from idle speed to a preselected "rotation" speed with constant angle of attack simulating the ground roll, after which the wind tunnel speed is maintained constant and the wing model is rotated to a preselected angle of attack corresponding V_2. This situation is maintained for 30–60 s followed by decelerating the wind tunnel to a halt. During the wind tunnel run aerodynamic coefficients are measured, particularly the lift coefficient. The lift loss due to the contamination is then considered to be the main parameter to assess the effect of the contamination, based on the reasoning above.

To evaluate the effects of the secondary wave on the lift degradation, two different configurations were studied for both wing section models: slat extended and slat retracted. Speed V_2, which also was the rotation speed, was limited to 60 m/s by the wind tunnel practical maximum speed. The tested configurations, angles of attack, and corresponding lift coefficients for uncontaminated wing section models during the simulated takeoff sequence are collected in Table 2. The time used to accelerate the wind tunnel speed to 60 m/s was selected to be 30 s as per AAT [1]. The mean pitch rates during the rotation were $3°/s$ with variation of $\pm 0.3°/s$.

It is important to realize that the test campaigns for the two different wing section models were independent of each other and performed during different time periods: DLR-F15 during 2012–14 and HL-CRM-Mod during 2016–17. The primary objective of DLR-F15 test campaign was to study the anti-icing fluid effects in general and the secondary wave topic appeared as a spin-off of those tests. During the HL-CRM Mod test campaign the secondary wave studies were included in the program from the beginning. This is the reason for the somewhat unsuccessful selection of the slat retracted configuration of the DLR-F15 wing section. As a slat increases the stall angle of attack, whereas a flap produces an upward shift in the lift curve, an equal flap angle in DLR-F15 configurations would have led to lift coefficients close each other as in the case of HL-CRM Mod. This in turn would have improved the comparability of the results for the two DLR-F15

Table 2 Wing section configurations, angle of attacks, and lift coefficients

Wing section	Slat/flap angle	Ground roll α	Ground roll C_l	α at V_2	C_l at V_2	Uncert. C_l
DLR—F15	S11°/F5°	0°	0.54	8.0°	1.32	±0.006
DLR—F15	S0°/F0°	0°	0.45	8.0°	1.22	±0.006
HL-CRM Mod	S22°/F10°	0°	0.52	9.2°	1.50	±0.008
HL-CRM Mod	S0°/F10°	0°	0.52	9.2°	1.49	±0.008

configurations with each other. Also, some of the additional tests done with the HL-CRM Mod were never performed afterward with DLR-F15. However, as the DLR-F15 tests contained relevant secondary wave–related results, they were included in the present study.

VI.　Results and Discussion

A.　Uncontaminated Wing Model Aerodynamics

The attainable range of lift coefficients for the takeoff simulation tests was a tradeoff between contradicting requirements. There was a need for a chord large enough to reach reasonable Reynolds number. Also, the slot dimensions for flaps and slats had to be large enough to get the fluids flowing without clogging. The restricting factor was the balance limit load (with a reasonable margin) for the lift force. This constrained the maximum lift coefficient during the tests to be below the ideal value corresponding the safety speed V_2 in a full-size airplane.

For the same reason, it was impossible to reach the stall with rotation speed of 60 m/s. Stall with lower speeds would have led to considerably lower Reynolds numbers and an inconsistent anti-icing fluid behavior. As the chord of the model was large relative to the wind tunnel test section the stall situation was not considered to be risk free, regarding the wind tunnel diffusor flow. The lift coefficient variations with angle of attack for the wing section models in slat extended configurations are presented in Fig. 4. Though both models were equipped with somewhat similar endplates, the lift coefficient slope of HL-CRM Mod wing section seems to be steeper. However, there is some nonlinearity in HL-CRM Mod slope too.

B.　Reynolds Number Considerations

The research work that formed the scientific basis for AAT included also considerations of the Reynolds number effects when using scaled wind tunnel models for fluid related tests. However, the AAT does not include any Reynolds number corrections or considerations per se. The research work and reasoning behind the AAT is thoroughly reviewed by Broeren and Riley [10].

Runyan et al. [12] discuss the fluid-related wind tunnel test limitations of the 3D 9.1% half model (average chord 0.3 m) and the 2D wing section model (chord 0.457 m) they used in their research as follows ([12] p. 5): "*Thus both models had short chords. This results in shorter fluid flow distances in the wind tunnel than on the full-scale airplane. Another effect of the short chords is lower chord Reynolds number in the wind tunnel, which results in higher shearing stress at a given percentage of the chord at a given velocity than is present on the full-scale airplane. We realized before the test that these differences would raise questions about the validity of the wind tunnel results. However, having flight data available for comparison with the wind tunnel data allowed the magnitude of these effects to be determined. It also provided the possibility, if it had been found necessary, of adjusting the wind tunnel parameters, such as fluid depth, tunnel speed, and velocity at rotation, to provide a better*
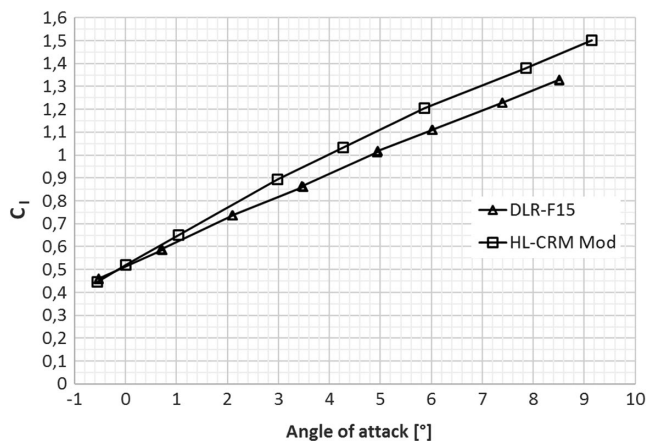
match with flight data. A parametric study was conducted of these variables, and adjustments were found to be unnecessary."

The chords of the two wing sections of present study are comparable with the chord of the 2D wing section model used by Runyan et al. [12]. Because there are presently no means to assess the effect of Reynolds number or other scaling effects in the fluid-related tests, it is assumed in the present study that the paradigm adopted by Runyan et al. is also valid for the secondary wave phenomena and its effects on lift loss.

C.　Visual Observations Slat Extended

1.　Wing Section Upper Surfaces

The following description of general visual observations on fluid behavior on the upper surface of the wing section applies to both wing section models. The photographs below are taken from the DLR-F15 tests due to the white paint on the surface that makes the fluid layer more visible.

During all fluid test runs, video recordings were taken to analyze the wave formation and the fluid flow off. The behavior of fluid flow off followed the general pattern of events described for a one element wing section model in [16]. However, the flow off begins at the trailing edge somewhat earlier than in the one-element model of [16] as there is airflow also in the slot between the flap and the wing main element. The first waves during the acceleration phase appeared near the mountings of the model, probably due to the local flow acceleration around the fittings (Fig. 5).

First waves in the midspan area (Fig. 5) of the wing section appeared at a wind tunnel speed of 11–15 m/s, which is quite close to the results of [16] (10–13 m/s). The wave onset speed or its variation from test to test did not depend on the wing section model tested. Most of the wing main section is clear of the fluid when the speed has reached 60 m/s, just before rotation (Fig. 6). At this point, there is still a visible fluid layer at the trailing edge area on both wing sections. The fluid at the trailing edge area will, however, diminish progressively after the rotation.

Within 1 s after the start of rotation a secondary flow wave appears from the upper side slat opening. The secondary wave is visible in Fig. 7 at a 47–50% chord position. In Fig. 8 there is a graphical presentation of the secondary wave movement for both wing section models. The average speed of the secondary wave is 7% of chord per second. This means that the secondary wave reaches the trailing edge area within about 10 s after the start of rotation. It is essential to note that the secondary wave appears from the slat cavity already at the start of rotation. As the rotation stops the secondary wave has already proceeded for more than 30% of the chord.

Figure 9 illustrates the fluid layer decrease at the flap area after rotation. It is important to note that the diminishing of the fluid after rotation supports the presumption of an attached flow condition at the trailing edge area. In case of flow separation at the flap area the fluid flow would either stop or even reverse.

2.　Wing Section Lower Surfaces

While the events on the upper surface of the two wing section models during the fluid flow-off process are practically identical, the fluid flow on the lower surface differs between the two models. The difference of the fluid flow on the lower surface is related to the different slat geometries between the wing section models. As seen in Fig. 1 there are two main differences in the slat geometries of the wing section models:

1) The relative size of DLR-F15 slat is clearly larger than that in the HL-CRM Mod.

2) As the selected slat angle of HL-CRM Mod is twofold compared with the DLR-F15, the lower surface of the slat is farther down from the wing section lower surface on HL-CRM Mod wing section than on DLR-F15 wing section.

When comparing the fluid flow on the lower surface of the two wing sections, there are two features that probably affect the differences in the secondary wave formation:

1) The larger slat of DLR-F15 collects by capillary effect clearly more fluid on the slat lower surface than the slat of HL-CRM Mod.

Fig. 4　Lift coefficient variation with angle of attack at speed of 60 m/s (Re 2.8×10^6). Wing section configurations—DLR-F15: slat 11°, flap 5°; HL-CRM Mod: slat 22°, flap 10°.
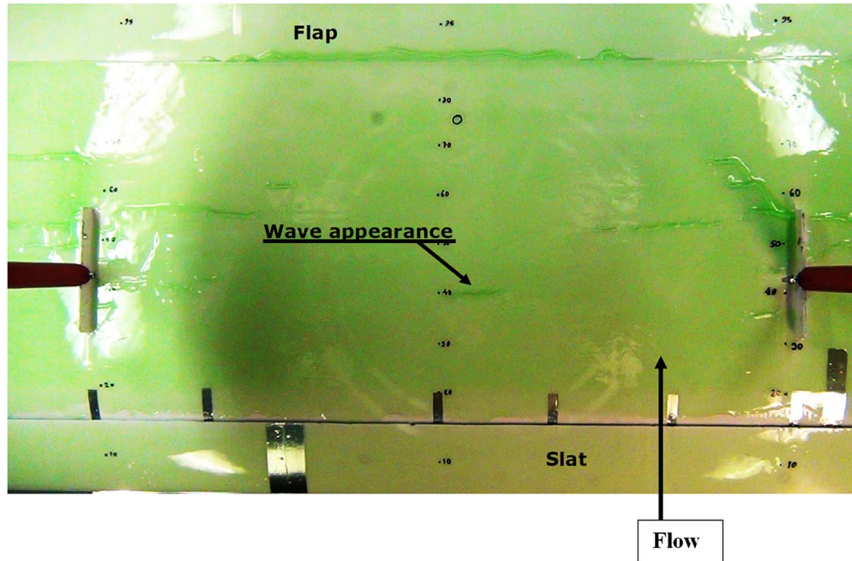
Fig. 5 Wave appearance in the midspan area at position $x/c = 40\%$.
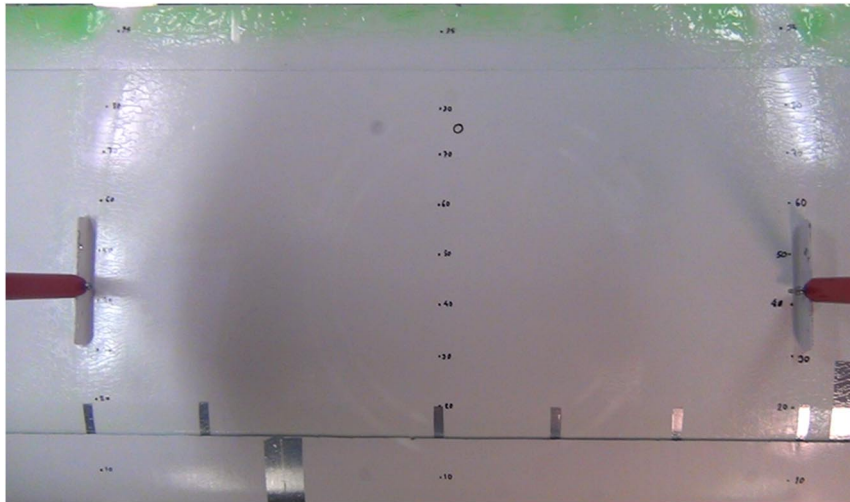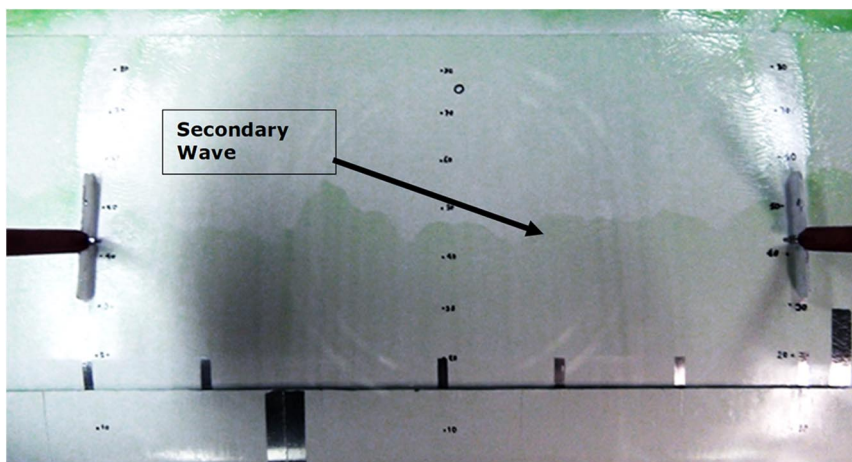

Fig. 6 Fluid distribution just before rotation.

Fig. 7 Secondary wave at a chord position of 47–50%. Note that the color, contrast, and brightness of the video frame are strongly modified using an image manipulation software to make the secondary wave more visible.

2) When the fluid flies off the slat lower surface during the acceleration phase, the fluid drop pattern differs significantly between the two wing sections.

During the acceleration phase, as the slat lower surface in the DLR-F15 wing section is closer to the main wing element, compared with HL-CRM Mod, the slat collects more fluid in the vicinity of the
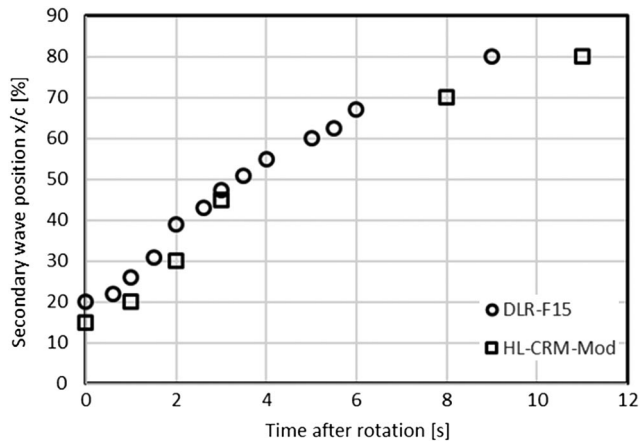
Fig. 8   Secondary wave movement along the wing section chord for both wing section models.

Fig. 10   The accumulation of fluid and wing section main element stagnation line during the acceleration phase.

stagnation line of the main wing element lower surface. In the case of HL-CRM Mod wing section, the fluid from the slat impinges on the wing main element farther downstream spreading the fluid more evenly over the lower surface. The amount of fluid accumulated near the main element lower surface stagnation line is thus less for the HL-CRM Mod wing section than for the DLR-F15. The visual observations of the secondary wave sizes support this assumption.

When rotation starts, the fluid collected in the vicinity of the slat opening during the acceleration phase moves via the slat cavity to the upper surface of the wing main element to form the secondary wave as the local flow conditions in the slat cavity change. The situation is illustrated schematically for DLR-F15 wing section in Fig. 10.

To isolate the secondary wave effect, an additional test run was performed with fluid treatment on the slat area only while the rest of the wing was left clean and dry. The videotape for this run revealed a secondary wave similar to the one in the test with full fluid treatment over the whole wing section chord.

D.   Visual Observations Slat Retracted and Sealed

The lift loss effects of the secondary wave have in previous studies often been related to the slat cavity. As already mentioned above, Runyan et al. [12] observed that for Boeing 737-200 ADV wing section the secondary wave in flap 15° configuration was associated with clearly higher lift loss compared with the configuration flap 5° with slat opening sealed. However, as revealed by Broeren et al. [13] the secondary wave may also appear on a slat less hard leading edge wing section.

To verify the secondary wave formation mechanism the two wing section models were tested in the present study also with slat retracted configuration. To prevent any leakage through the slat opening the slat was sealed. The slat retracted, and sealed configurations tested were as indicated in Table 2.

Both wing sections were videotaped from the upper and lower side. The upper-side video tape showed no signs of any secondary wave for
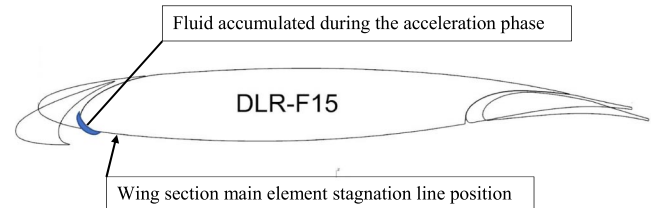
either wing section. On the lower surface of the wing section there was no accumulation of fluid indicated around the stagnation line during the acceleration phase as was for the slat extended configuration. The fluid flowed off evenly on the lower surface during the acceleration phase. After rotation, the fluid flow continued as before rotation and there was only a slight movement of the stagnation lines without any accumulated fluid visible in both wing section models.

E.   Lift Degradation and Pitching Moment Results

Before each test with anti-icing treatment, the uncontaminated wing sections for different configurations were measured to eliminate different daily changing factors on the results. As stated earlier, the uncontaminated wing section results were quite well repeatable, whereas the anti-icing treatment led to less repeatable results. The noise levels of measured lift coefficient after anti-icing treatment were clearly higher than that for the uncontaminated wing case up to the end of each test run.

In the sections below, the lift degradation analysis is divided into the comparison of the lift slope curves measured during the rotation phase and to the relative lift degradation after rotation by comparing secondary wave movements and lift degradations over time.

In Fig. 11 the lift slope during the rotation phase is illustrated for DLR-F15 wing section in two different configurations—slat extended and retracted. Worth noticing in Fig. 11 is the difference between anti-iced and uncontaminated lift slopes for slat extended and slat retracted configurations. In slat retracted configuration the difference between the lift coefficients is reducing with angle of attack, while for the slat extended configuration the lift coefficient difference is slightly increasing with angle of attack. As there is no fluid transferred from the lower surface to the upper surface in slat retracted (and sealed) configuration the prevailing fluid thickness is reducing in time throughout the simulated takeoff sequence, whereas the replenishment of the fluid from the lower surface to the upper surface forms the secondary wave, which affects the lift coefficient in slat extended configuration during the rotation phase.

Figures 12 and 13 illustrate the fluid contamination effect on the DLR-F15 pitching moment coefficient for two different configurations—slat extended and retracted. The fluid contamination causes for both configurations a reduction in nose down pitching moment. This is most probably due to the growth of boundary-layer displacement thickness, which in turn leads to an effective
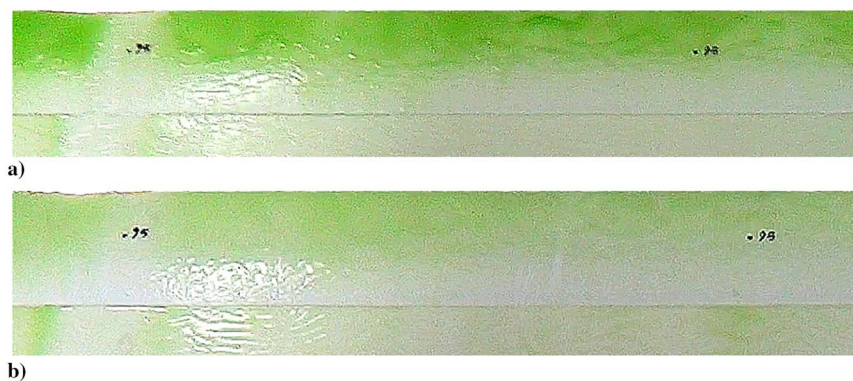

Fig. 9   Fluid layer at flap area a) immediately after rotation and b) 30 s after rotation.
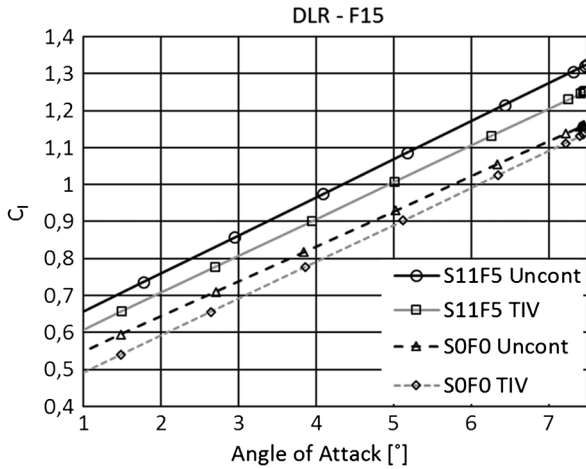
Fig. 11 Lift coefficient slope during the rotation of DLR-F15 for uncontaminated and anti-icing fluid–treated wing section models with configuration slat 0°, flap 0°, and slat 11°, flap 5°.
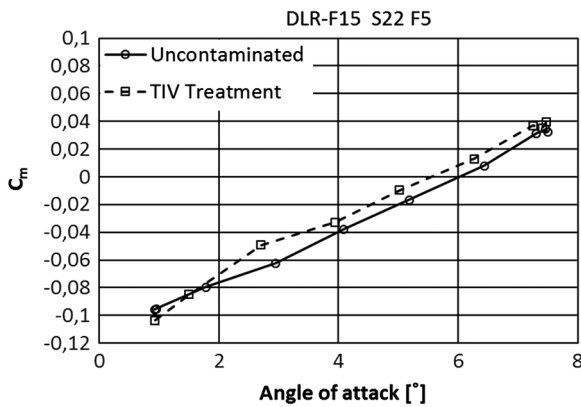

Fig. 12 Pitching moment coefficient variation with angle of attack for DLR-F15 slat extended configuration.
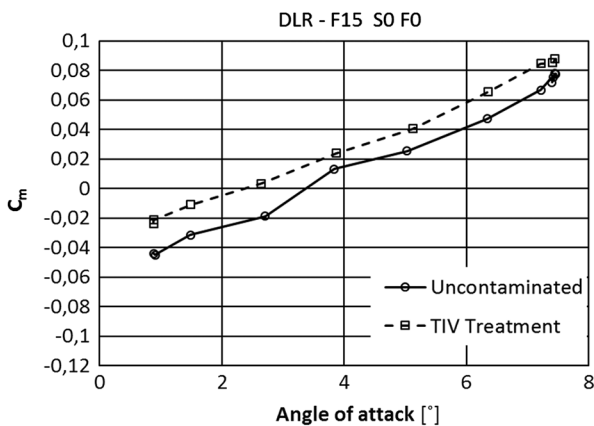

Fig. 13 Pitching moment coefficient variation with angle of attack for DLR-F15 slat retracted configuration.
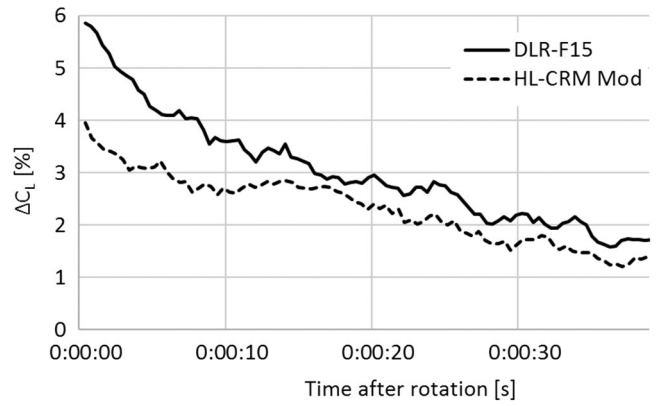

Fig. 14 Comparison between the relative lift coefficient degradations in percentage of the uncontaminated lift coefficients of the DLR F-15 (slat 11°, flap 5°) and HL-CRM Mod (slat 22°, flap 10°) wing sections. Both wing sections are treated with type IV fluid.

decambering of the wing sections. The decrease in nose down pitching moment is clearly smaller for the slat (and flap) extended than for the slat (and flap) retracted configuration. This may be due to the smaller relative effect of boundary-layer displacement thickness caused decambering in the slat and flaps extended configuration. The absolute values of pitching moments support this reasoning. This kind of a difference between uncontaminated and fluid contaminated wings may be observed also in [12] when comparing pitching moment in flaps 5° and flaps 15° configurations in the 3D half model.

Unfortunately, these results are not presented for the 2D wing section model in [12].

The nearly linear behaviors of the pitching moment plots in Figs. 12 and 13 suggest that there is no evidence on boundary-layer separation during the rotation.

To evaluate the contribution of the secondary wave in the lift loss, its variation in time after rotation is considered in the following sections. Figure 14 compares the anti-icing treatment–induced relative lift degradation in time after rotation for the two wing section models in slat extended configuration. The lift loss is expressed as percentage of the uncontaminated lift coefficient. As noticed before, the secondary wave was observed on the wing upper surface for both models after rotation in slat extended configurations. In addition, there was visual evidence for a weaker secondary wave in the HL-CRM Mod model compared with the DLR-F15 model due to a smaller amount of fluid accumulated on the lower surface of HL-CRM Mod during the acceleration phase.

Two facts may be observed in Fig. 14. There is a significant difference in lift loss values immediately after rotation between the two wing sections. For both wing sections, however, the largest lift loss occurs during the 10 s interval after rotation. Comparing this decrease to the secondary wave movement along the wing section chord in time (Fig. 8) the relationship between secondary wave position and lift loss in time becomes evident. The roughness induced lift loss is, according to several studies related strongly to the roughness element distance from the leading edge [17]. As the secondary wave moves downstream towards trailing edge the wave related lift loss therefore reduces. This suggests that the higher values of lift loss during the 10 s interval after rotation are caused by the secondary wave.

As noticed above, there were no signs of secondary waves in either wing section model with slat retracted configuration, whereas clear secondary waves were present for both wing section models when slats were extended. Isolation of the secondary wave effect is considered in the following by comparing the lift losses between these two configurations. In Fig. 15 the anti-icing fluid–induced lift loss variation in time is illustrated for DLR-F15 wing section in the two different configurations. As the flap angles in slat extended and retracted configurations are not identical in case of DLR-F15 the comparison of lift losses is somewhat problematic. The uncontaminated lift coefficients for the two configurations are probably too far away from each other to justify a direct comparison between these two configurations.

The large absolute difference in lift losses between the different configurations of DLR-F15 is difficult to prove to be an effect of secondary wave per se. The lift loss difference time history (Fig. 15) may, however, reflect the secondary wave effect. If the lift losses for the two DLR-F15 configurations were induced by a similar kind of primary wave phenomena, the lift loss difference between these two could be assumed to be nearly constant in time. The difference in lift losses between slat extended and slat retracted configurations in Fig. 15 halves within the first 12 s, which after it remains at the same
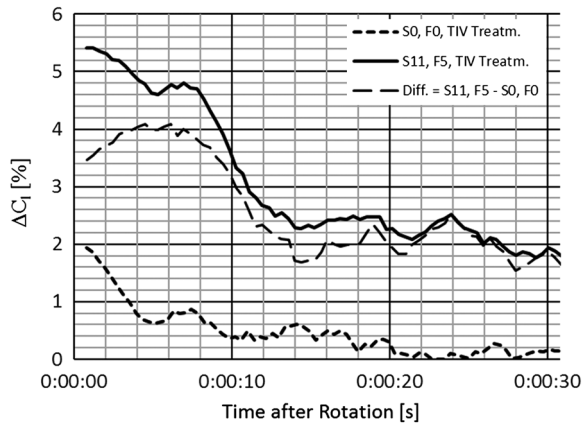
Fig. 15   Lift degradation after rotation for slat extended and retracted configurations in DLR-F15 wing section. Both configurations are treated with type IV fluid.

level for at least the next 14 s. The secondary wave on the wing upper surface is shown in Fig. 8 to be within 10 s from the rotation at position $x/c = 0.8$. It may then be assumed that the secondary wave effect is vanished within the time when the above-mentioned difference of lift losses has leveled off from the initial value of 4% to approximately 2%. This reasoning suggests that the secondary wave effect is approximately reflected by the difference in lift losses between slat extended and slat retracted configurations in Fig. 15.

For the HL-CRM Mod wing section model the comparison between the slat extended and slat retracted configurations is more appropriate than for the DLR-F15. Considering generally the linear region of the lift slope for a three-element wing section, equal flap angles for slat extended and slat retracted configurations gives approximately equal lift coefficients as illustrated by van Dam in [18] (Fig. 1). This applies also for HL-CRM Mod as shown in Table 2.

The anti-ice fluid–related lift loss variations in time after rotation for slat extended (secondary wave present) and slat retracted (no secondary wave) configurations are presented for HL-CRM Mod wing section in Fig. 16. The largest lift loss difference between the two different slat configurations occurs during the 10 s interval after rotation. This lift loss difference variation in time reflects again the secondary wave position in time (Fig. 8).

To further isolate the secondary wave effect, an additional test was performed for HL-CRM Mod. In this test anti-icing fluid was applied on the slat area only. Because of the slant position of the slat, the initial fluid thickness on the slat area was not more than 0.5 mm. However, the run off fluid from the slat cavity to the lower surface was sufficient to form a clearly observable secondary wave.

When summing up the lift losses for slat retracted configuration—primary wave only—and slat extended with fluid application on slat
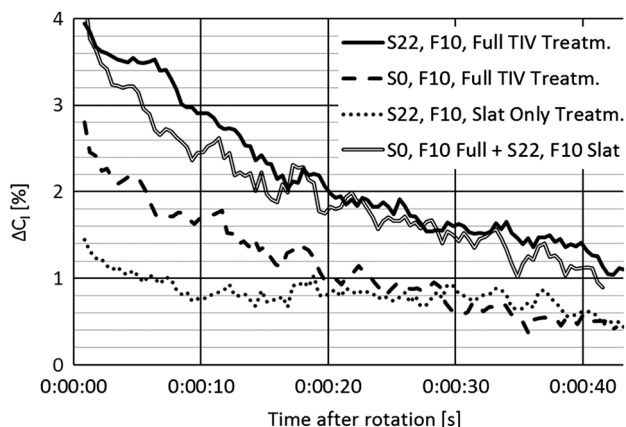
area—secondary wave only—the resulting plot is close to the slat extended configuration with full fluid treatment as illustrated in Fig. 16. If the linear superposition of the two separate fluid contamination types is accepted the reasoning above suggests that the lift loss for HL-CRM Mod wing section, at the point of rotation, with secondary wave present is about 1.5-fold compared with the lift loss without the secondary wave.

There were two tests carried out with a fixed sand paper roughness with height $k = 0.6$ mm or $k/c = 0.96 \times 10^{-3}$ attached to the area immediately after the slat upper opening (corresponding relative position of $x/c = 0.1$–0.15), to simulate the secondary wave just after rotation. The width of the sand papers were 50 and 100 mm. The selected thickness of the sand paper was based on a bare eye estimate of fluid thickness as no accurate method for fluid thickness determination was available. The sand paper width was chosen to be in accordance with the secondary wave position just after rotation (Fig. 8). The lift losses induced by these roughness elements and the lift loss immediately after rotation in the test where slat only was applied with anti-icing fluid were as follows:

1) Sand paper 50 mm: $\Delta C_l = 1.26\%$.
2) Sand paper 100 mm: $\Delta C_l = 1.63\%$.
3) Slat only anti-icing: $\Delta C_l = 1.65\%$.

The sand paper and isolated secondary waves are comparable roughness elements as the rest of the surface is uncontaminated, before the secondary wave has traveled over the wing section chord. In the sand paper roughness tests, the lift coefficient and pitching moment coefficient variations with angle of attack differed from the uncontaminated cases in a similar manner as in the fluid contaminated DLR-F15 tests with slat extended configuration (Figs. 11 and 12). This suggests that the lift degradations induced by the sand paper, as well as by the secondary wave, are caused by the increased boundary-layer displacement thickness and the following effective decambering of the wing section due to the upper surface roughness.

F.   Previous Research and Underlying Flow Phenomena

As mentioned above Runyan et al. [12] discovered that the fluid contamination–caused lift loss values in B737-200 ADV wing section model are higher for flaps 5° configuration compared with flaps 15° configuration, which accompanied a larger secondary wave than flaps 5° configuration. For two different anti-ice fluids, the lift losses at $\alpha = 8°$ were 1.15- to 1.29-fold ($-10°C$) and 1.21- to 1.41-fold ($-20°C$) for flaps 15° configuration compared with flaps 5° configuration. The differences may be considered as significant. However, the difference between the smaller and larger secondary wave is left vague due to qualitative assessment of the waves. The lift loss and pitching moment changes are according to Runyan et al. based on fluid contamination caused thickening of boundary-layer thickness, which in turn reduces the effective camber of wing section models.

Broeren et al. [13] give an extensive analysis on the underlying flow phenomena causing the lift and pitching moment alterations due to fluid and fixed contamination. Of interest is particularly whether the changes in lift and pitching moment are caused by leading edge separation bubble, flap area flow separation, or by the boundary-layer displacement thickness growth and the subsequent effective decambering of the wing section. It is important to note that [13] considers the contamination related lift losses and pitching moment changes up to the stalling angle of attack. Broeren et al. conclude the following: "*In the linear portion of the lift curve the primary aerodynamic effect was the thickening of the downstream boundary layer due to accumulation of fluid and contamination. This causes a reduction in lift coefficient and increase in pitching moment (nose up) due to an effective decambering of the wing.*"

Considering all the contamination-caused lift losses in the present study, they are assumed to be a consequence of downstream thickening of boundary-layer displacement thickness, and the subsequent reduction of effective camber of the wing sections referred to above. This assumption is based on the following observations:

1) The maximum angle of attack values during the tests for both wing section models were clearly within the linear region of the lift slope.

Fig. 16   Lift degradation after rotation for slat extended and retracted configurations for HL-CRM Mod wing section after type IV fluid treatment.

2) Based on video recordings of the fluid movement during the tests, there are no signs of flow separation or separation bubbles along the upper surface of the two wing sections—especially the fluid reduction at the flap area is progressive without disturbances up to the end of the test runs, which indicates an attached boundary layer throughout the tests.

3) The pitching moment curves for fluid-contaminated wing sections show quite even increase (nose up) compared with the uncontaminated wing sections, without any distinct difference in curve shape, which in turn would indicate a local flow separation.

VII. Conclusions

The main objectives of this study were to evaluate quantitatively the contribution of the secondary wave in the anti-icing fluid–induced lift degradation at the point of lift-off, and to estimate the effect of wing section geometry on the formation of the secondary wave. Two wing section types were used with two different configurations. One type IV anti-icing fluid was used in all fluid-related wind tunnel tests. In addition, two tests were accomplished using fixed sand paper type of roughness to simulate the anti-icing fluid–induced roughness on the upper surface of the wing section.

Main findings of the tests were as follows:

1) For the two wing section models tested, secondary waves were observed only in the slat extended configurations.

2) The fluid accumulation process on the lower surface during the acceleration phase differed between the two wing section models in slat extended configuration. Visual qualitative observations indicated a smaller secondary wave on the HL-CRM Mod wing section when compared with the DLR-F15 wing section.

3) Visual observations supported the assumption that slat size and geometry influence the formation and size of the secondary wave.

4) For the two wing sections tested the configurations with secondary wave present were estimated to induce at least 1.5-fold lift losses compared with the configurations without secondary wave. Though the exact numerical contribution of the secondary wave in the lift loss was impossible to isolate precisely, it was obvious that the secondary wave increases considerably the lift loss caused by the anti-icing fluid.

The results of present study suggest that the secondary wave effects on the lift loss of a wing section are strongly wing section geometry dependent. The relative size and position of the slat in the wing section has an obvious effect on the fluid accumulation on the lower surface of the wing section during the acceleration phase, and on the size of the subsequent secondary wave after rotation.

Acknowledgments

References

[1] SAE Aerospace Standard, "Standard Test Method for Aerodynamic Acceptance of SAE AMS 1424 and SAE AMS 1428 Aircraft Deicing/Anti-Icing Fluids," AS5900 Rev. C, SAE International, Oct. 2016.

[2] Hendrickson, G. S., and Hill, E. G., "Effects of Aircraft De-/Anti-Icing Fluids on Airfoil Characteristics," von Karman Inst. For Fluid Dynamics Lecture Series "Influence of Environmental Factors on Aircraft Performance", von Karman Inst. for Fluid Dynamics, Brussels, Belgium, Feb. 1987.

[3] Cruse, D. L., and Zierten, T. A., "Boeing/Association of European Airlines (AEA) Evaluation of the Aerodynamic Effects of Aircraft Ground De-/Anti-Icing Fluids," *Society of Flight Test Engineers 19th Annual Symposium*, Arlington, TX, Aug. 1988.

[4] Runyan, L. J., Zierten, T. A., and Hill, E. G., "Flight and Wind Tunnel Investigation of Aerodynamic Effects of Aircraft Ground Deicing/Anti-Icing Fluids," *AGARD Conference Proceedings No. 470, Flight in Adverse Environmental Conditions*, Gol, Norway, May 1989, pp. 24-1–24-11.

[5] Carbonaro, M., "Experimental Study of the Flow of a Film of Aircraft Deicing Fluid During a Simulated Take Off at Subfreezing Temperature," von Karman Inst. for Fluid Dynamics CR 1985-02, Brussels, May 1985.

[6] Carbonaro, M., "Experimental Study of the Aerodynamic Characteristics of a Two-Dimensional Wing Model Covered with De/Anti-Icing Fluid During a Simulated Take Off at Subfreezing Temperature," von Karman Inst. for Fluid Dynamics CR 1986-22, Brussels, Aug. 1986.

[7] Carbonaro, M., "Further Study of the Aerodynamic Performance of a 2-D Wing Model Covered with Simulated Frost or with De/Anti Icing Fluid During a Simulated Take Off at Subfreezing Temperature," von Karman Inst. for Fluid Dynamics CR 1987-29, Brussels, July 1987.

[8] Ellis, N. D., Nettleton, T. R., and Eggleston, B., "Effects of Anti-Icing/De-Icing Fluids on the Take-Off Performance of Commuter Aircraft," Rept. DHC-TDC-90-1, Transport Canada De Havilland, March 1991.

[9] Louchez, P. R., Laforte, J. L., and Bouchard, G., "Boundary Layer Evaluation of Anti-Icing Fluids for Commuter Aircraft," Rept. TP11811E, Transport Canada, Dec. 1994.

[10] Broeren, A. P., and Riley, J. T., "Review of the Aerodynamic Acceptance Test and Application to Anti-Icing Fluids Testing in the NRC Propulsion and Icing Wind Tunnel," NASA TM 2012-216014, DOT/FAA/TC-12/32, Aug. 2012.

[11] Hill, E. G., and Zierten, T. A., "Aerodynamic Effects of Aircraft Ground Deicing/Anti-Icing Fluids," *Journal of Aircraft*, Vol. 30, No. 1, Jan.–Feb. 1993, pp. 24–34.
doi:10.2514/3.46301

[12] Runyan, L. J., Zierten, T. A., Hill, E. G., and Addy, H. E., "Lewis Icing Research Tunnel Test of the Aerodynamic Effects of Aircraft Ground Deicing/Anti-Icing Fluids," NASA TP 3238, Aug. 1992.

[13] Broeren, A., Lee, S., and Clark, C., "Aerodynamic Effects of Anti-Icing Fluids on a Thin High-Performance Wing Section," *Journal of Aircraft*, Vol. 53, No. 2, March–April 2016, pp. 451–462.
doi:10.2514/1.C033384

[14] Wild, J., "Experimental investigation of Mach- and Reynolds-Number Dependencies of the Stall Behavior of 2-Element and 3-Element High-Lift Wing Sections," *50th AIAA Aero-Space Sciences Meeting Including the New Horizons Forum and Aerospace Exposition*, AIAA Paper 2012-0108, Jan. 2012.

[15] Lacy, D. S., and Sclafani, A. J., "Development of the High Lift Common Research Model (HL-CRM): A Representative High Lift Configuration for Transonic Transports," AIAA Paper 2016-0308, Jan. 2016.

[16] Koivisto, P., "Anti-Icing Fluid Flow Off on a Wing Section During Simulated Taxi and Take-Off," *5th Atmospheric and Environments Conference*, AIAA Paper 2013-2932, June 2013.

[17] Lynch, F. T., and Khodadoust, A., "Effects of Ice Accretions on Aircraft Aerodynamics," *Progress in Aerospace Sciences*, Vol. 37, No. 8, 2001, pp. 669–767.
doi:10.1016/S0376-0421(01)00018-5

[18] van Dam, C. P., "The Aerodynamic Design of Multi-Element High-Lift Systems for Transport Airplanes," *Progress in Aerospace Sciences*, Vol. 38, No. 2, 2002, pp. 101–144.
doi:10.1016/S0376-0421(02)00002-7